

Iridescent colored bands on clouds

PHILIP LAVEN¹ AND LEN HALL²

¹ 9 Russells Crescent, Horley, RH6 7DJ, UK

² 541 W. Hackney Ave, Trlr B1, Globe, AZ 85501, USA

* Corresponding author: philip@philiplaven.com

Abstract: Iridescence on clouds is often considered to be closely-related to the rings of the atmospheric corona. Both phenomena are caused by near-forward scattering of sunlight. The colored rings of the corona are caused by diffraction from water droplets of fairly uniform size. Iridescence is often seen as bands of color along the edges of clouds. Mie theory shows that near-forward scattering of sunlight is a complicated function of droplet radius r and scattering angle θ . It is difficult to analyze photographs of iridescence because most photographers deliberately exclude the Sun and, hence, we do not know the value of θ . This paper uses indirect techniques to determine the relative position of the Sun, thereby revealing θ and allowing estimates of the droplet radius r at different points in the iridescent clouds. The results demonstrate that variations in r produce the narrow bands of color aligned with the edges of clouds.

1. INTRODUCTION

Iridescent bands of color frequently appear along the edges of clouds, but the causes of such effects need to be thoroughly investigated. This paper analyzes various photographs of iridescent clouds by using Mie theory calculations for near-forward scattering of sunlight to determine the sizes of cloud droplets.

In November 2021, Len Hall observed some iridescent clouds near Montpelier, Idaho, USA. He took a series of still photographs over a period of about 30 minutes: one example is given as Fig. 1(a). Although the iridescence was clearly visible to the naked eye, it was barely visible in most of his images. However, increasing the color saturation by 300% (using the color saturation feature in Microsoft PowerPoint) revealed a complicated pattern of reddish bands along the edges of the clouds, as shown in Fig. 1(b).

Cloud iridescence is closely-related to the atmospheric corona. Both phenomena are caused by near-forward scattering of sunlight by spherical water drops in clouds. The circular rings of the corona can be explained using diffraction theory [1,2] but iridescence is much more complicated since it often appears as bands of color along the edges of clouds or as haphazard patches of color which do not seem to follow any regular pattern.

As photographs of iridescence typically exclude the Sun, scientific analysis is hampered by not knowing the angular separation from the Sun. This paper outlines two indirect methods to overcome this problem, thus allowing us to estimate the sizes of cloud droplets.

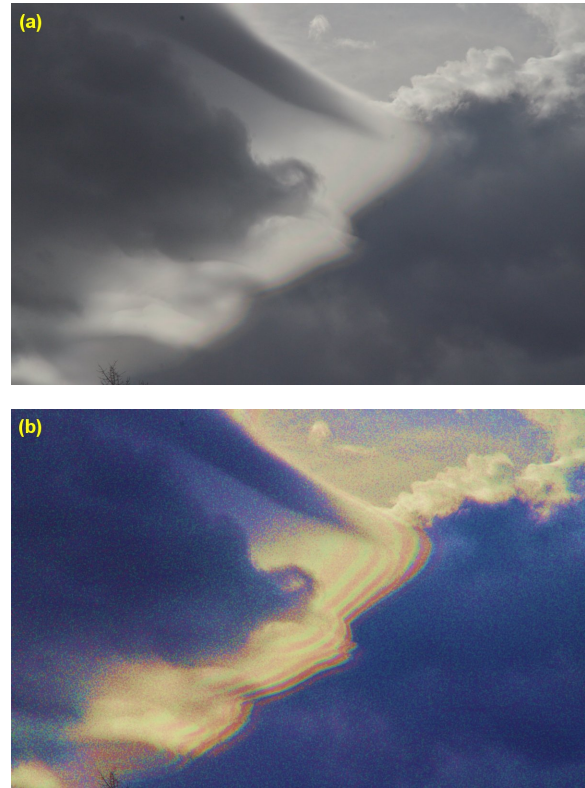


Fig. 1(a) shows the unprocessed image of iridescent clouds recorded at 1242 on 14 November 2021 © Len Hall. Image (b) shows the effect of the increasing the color saturation of image (a) by 300%.

Section 2 of this paper reviews the differences between the results of diffraction theory and Mie theory for near-forward scattering of sunlight. [3-8] Section 3 examines a photograph of bright iridescence on clouds in which the position of the Sun can be inferred by the convergence of radial shadows. Section 4 is based on detailed analysis of a series of photographs (such as Fig. 1) which benefited from a contemporaneous set of wide-angle images taken by a tripod-mounted camera.

2. NEAR-FORWARD SCATTERING

Near-forward scattering of sunlight by spherical droplets of water in clouds can be simulated by diffraction calculations as shown in Fig. 2(a) and Mie theory calculations as shown in Fig. 2(b).

The diagrams in Figs. 2(a) and (b) were calculated using 300 equally-spaced wavelengths between 380 and 700 nm. The spectrum of sunlight took account of atmospheric absorption, assuming that the elevation of the Sun was 40°. The diffraction calculations are independent of refractive index, whereas the Mie calculations used the IAPWS values for the refractive index of water at 5°C. [9] As the scattered intensity varies by many orders of magnitude as r is increased from $r = 0.1 \mu\text{m}$ to $r = 20 \mu\text{m}$, the resulting RGB values at (r, θ) were converted to saturated colors by multiplying the individual R, G and B values by a factor that results in the highest value being 255.

Although diffraction calculations are an approximation, they provide a simple explanation for the colored circular rings of the corona. [1,2] As the axes used in Fig. 2 are logarithmic, the three inner red rings of the corona are represented by straight lines defined by $\theta \approx 16/r$, $31/r$, and $47/r$, where the scattering angle θ is measured in degrees and the droplet radius r is measured in micrometers.

The results of Mie theory calculations shown in Fig. 2(b) are similar to the results of diffraction calculations when $r > 5 \mu\text{m}$, but they disagree dramatically when $r < 3 \mu\text{m}$. [4, 8] In particular, the near-vertical lines at the top of Fig. 2(b) indicate areas where the color of the scattered light is almost independent of θ , but critically dependent on r . This anomaly suggests that the color of scattered sunlight could be used as a very sensitive indicator of droplet radius r when $0.6 \mu\text{m} < r < 3 \mu\text{m}$ and $\theta < 10^\circ$.

Fig. 2(b) also shows some very complicated patterns when $1 \mu\text{m} < r < 4 \mu\text{m}$ and $\theta > 8^\circ$. They are probably responsible for the haphazard patches of color occasionally seen in iridescent clouds.

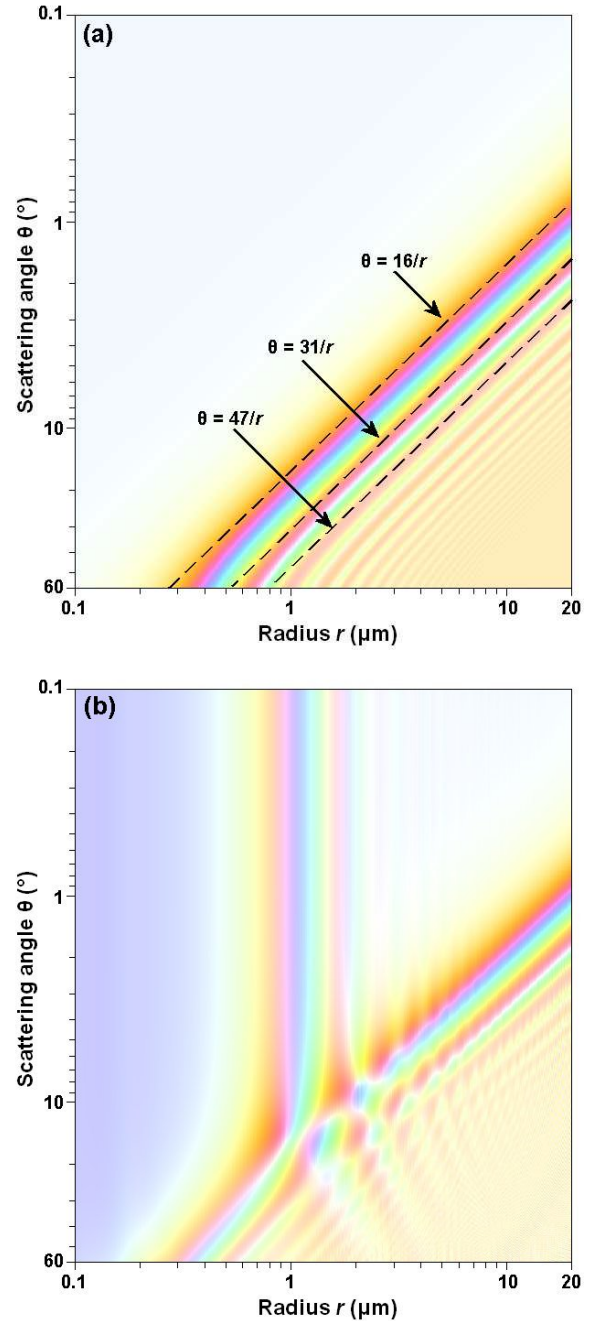


Fig. 2 Scattering of sunlight as a function of scattering angle θ and droplet radius r . (a) shows the results of diffraction calculations, whereas (b) shows the results of Mie theory calculations. As the relative intensity of the scattered light varies dramatically across the range of angles and droplet sizes, it is not possible to reproduce the full dynamic range of the scattered light. Hence, Fig. 2 displays only the saturated colors of the scattered light.

What causes these differences between Fig. 2(a) and (b)? van de Hulst used the term “anomalous diffraction” to mean the interference pattern between (a) light that has been diffracted by a water droplet and (b) light that is transmitted through a water droplet. [10] This interpretation is confirmed by Debye series calculations for the combination of $p = 0$ (diffraction plus external reflection) and $p = 1$ (transmission through the spherical droplet) as shown by Fig. 13 in [8] which shows exactly the same pattern of near-vertical colored lines as in Fig. 2(b).

3. INFERRING THE POSITION OF THE SUN

Due to the limited dynamic range of digital cameras, photographers often deliberately exclude the Sun from their images because it is so much brighter than the iridescence. Consequently, we rarely know whether photographs of iridescent clouds represent scattering at, for example, $\theta \approx 5^\circ$ or $\theta \approx 20^\circ$. An interesting exception is shown in Fig. 3(a) where the position of the Sun can be inferred by the converging shadow lines at the top right of the image. In this case, we can see that bright iridescence occurs when $4^\circ < \theta < 8^\circ$, with fainter iridescence up to $\theta \approx 15^\circ$.

Cloud droplets in lenticular clouds tend to be well-ordered in terms of size (with smaller droplets at the edges of clouds and larger droplets away from the edges of clouds) [4, 11-13]. In essence, very small droplets form in air entering clouds and then coalesce with other very small droplets as they move further into the cloud to produce larger droplets, which then coalesce with other droplets to produce even larger droplets, and so on. Our hypothesis is that the droplets of a specific size cause cloud iridescence to appear as bands of color aligned with the edges of clouds.

For individual points with pixel values (x, y) in Fig. 3(a), it is simple to calculate their angular separation θ from the Sun. Having chosen points corresponding to reddish areas in Fig. 3(a), we then transfer these points with the specified value of θ into reddish areas of Fig. 3(b) using the fact that droplet sizes tend to increase with distance from the edges of the clouds. As the pixel values in Fig. 3(b) correspond to (r, θ) , this process allows us to determine the droplet radius r .

The points marked A – F in Fig. 3(a) correspond to reddish iridescence: points A and C are very close to the edges of clouds, whereas points B, D, E and F are well away from the edges of clouds. The near-vertical nature of the bands in Fig. 3(b) indicate that r is fairly insensitive to the precise value of θ when $\theta < 10^\circ$. Using the principle that smaller droplets are likely to be near the edges of clouds, it seems reasonable to assume that the droplets selected in Fig.

3(a) correspond to the reddish bands in Fig. 3(b) at $r \approx 0.93 \mu\text{m}$ and $r \approx 1.77 \mu\text{m}$.

This assignment could be challenged on the basis that Fig. 3(b) contains other reddish bands such as that corresponding to $r \approx 2.4 \mu\text{m}$. Perhaps, the reddish bands in Fig. 3(a) are caused by droplets with $r \approx 1.77 \mu\text{m}$ and $r \approx 2.4 \mu\text{m}$? Fig. 3(b) shows that, when $\theta \approx 6^\circ$, the sequence of colors between $r \approx 0.93 \mu\text{m}$ and $r \approx 1.77 \mu\text{m}$ is red, purple, blue, cyan, green, yellow and red, whereas the sequence of colors between $r \approx 1.77 \mu\text{m}$ and $r \approx 2.4 \mu\text{m}$ is red, yellow, green, yellow and red. Careful examination of Fig. 3(a) shows that the color sequence between points marked A and C and the points marked B, D, E and F is consistent with our original assumption of $r \approx 0.93 \mu\text{m}$ and $r \approx 1.77 \mu\text{m}$.

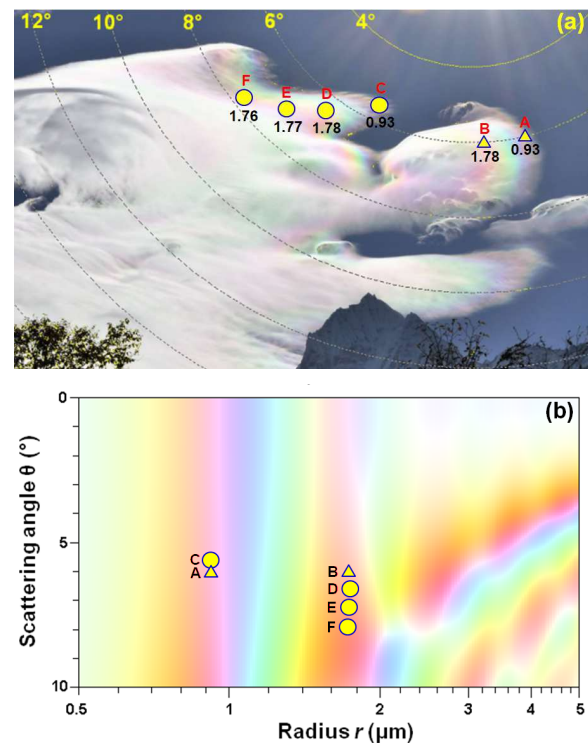


Fig. 3 (a) Photograph of iridescent clouds over Mt. Thamserku (6604 m) in the Himalayas on 18 October 2009. © Oleg Bartunov. The position of the Sun can be determined by the convergence of the faint shadow lines at the top right of this image. Points A – F correspond to reddish bands of color on the clouds. (b) Mie theory simulations for scattering of sunlight. Using the values of θ derived from (a), the points A – F have been re-plotted in (b), allowing us to estimate the droplet radii r (measured in μm) for each point, as shown in (a).

4. CALCULATING THE SUN'S POSITION

The near-vertical reddish lines in Fig. 3(b) mean that we do not need to know the precise values of θ when $\theta < 10^\circ$ to estimate the droplet radius r . As this simplification is not applicable when $\theta > 10^\circ$, some mechanism is needed to determine the values of θ corresponding to the various iridescent bands. An

interesting solution to this problem was used by Len Hall: his still images of cloud iridescence recorded by a hand-held camera with focal length of 128.2 mm (35mm equivalent) were accompanied by a contemporaneous set of wide-angle (focal length ≈ 32 mm) time-lapse images recorded at intervals of 2 seconds by a camera mounted on a leveled tripod.

Fig. 4 shows one of these time-lapse images, together with a small version of Fig. 1(a) taken at almost the same time. To get the best match with the clouds, this version of Fig. 1(a) has been rotated counter-clockwise by 2° . As the Sun was obscured by clouds throughout the 10-minute sequence of time-lapse images, it is not possible to determine directly its location from the wide-angle images. However, these images show various local landmarks (such as the spire of a church) at specific pixel values (x, y) . Using the equations given in the Appendix, if we know the elevation ϕ_1 and azimuth λ_1 of any of these local landmarks (as measured from the location of the tripod-mounted camera), we can calculate the elevation ϕ_0 and azimuth λ_0 of the aiming point of the camera, as defined by the center of the image (x_0, y_0) measured in pixels.

In practice, we found that this process gave significantly different results for ϕ_0 and λ_0 depending on which local landmark was selected as the origin of our calculations. This failure suggested that the nominal focal length of 32 mm might be incorrect. Consequently, a “star field” image was taken on a clear night. Analysis of 155 stars on this image revealed that the focal length was actually 34.77 mm. Using this new value of focal length, the values of ϕ_0 and λ_0 were much more consistent starting with different landmarks.

The next steps involved calculating the elevation ϕ_{Sun} and azimuth λ_{Sun} of the Sun at the time when Fig. 4 was taken – and then calculating the corresponding pixel values x_{Sun} and y_{Sun} . Lines plotted on Fig. 4 show the angular separation θ from the Sun centered on x_{Sun} and y_{Sun} , which also covered the inset image corresponding to Fig. 1(a). It is important to understand that these lines are not quite circular because of the effect of the mapping function of the lens.

It is also important to observe the multi-layer character of the clouds in Fig. 4. The dark cloud on the left of the inset is low cloud, a result of condensation in rising clear air. The light cloud with iridescence is high cloud, a lenticular cloud forming in air passing through the mountain wave from the right. New droplets form and grow as they are carried into the stationary wave cloud.

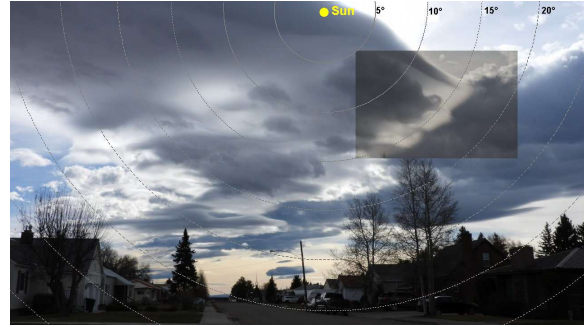


Fig. 4 One of the wide-angle time-lapse images, together with an inset version of Fig. 1(a).

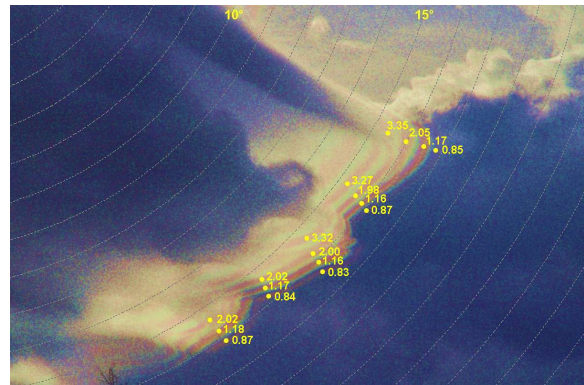


Fig. 5 As Fig. 1(b) except that it shows the angular separation θ from the Sun, as well as the estimated values of droplet radius r (in μm) at specific points on the iridescent bands.

As the position of the Sun varied during the 10 minutes of the time-lapse observation period, as well as the relative positions of images taken by the hand-held camera, composite images (such as Fig. 4) are used to show the position of the Sun and, more importantly, the angular separation θ from the Sun.

As mentioned earlier, cloud droplets typically increase in size as they move away from the edges of clouds. Consequently, for each series of three or four yellow dots shown in Fig. 5 with $15^\circ < \theta < 17^\circ$, we can estimate the values of r by plotting the points with $15^\circ < \theta < 17^\circ$ for each of the reddish bands in Fig. 2(b).

Fig. 6(a) shows another image in the series of photographs taken by Len Hall on 14 November 2021, whilst Fig. 6(b) shows the effects of increasing color saturation by 300%. It is again important to observe the multi-layer character of the clouds: the dark cloud on the left is low cloud, while the bright cloud with iridescence is high cloud formed in a mountain wave with the air flowing through it from right to left. Fig. 6(c) shows angular separation from the Sun, together with estimates of droplet radius r . In this case, iridescence is associated with values of θ between 5° and 12° . Careful examination of Fig 6(b) suggests that there are up to 6 colored bands. Fig.

6(c) shows that these bands are caused by droplets ranging from radius $r \approx 0.9 \mu\text{m}$ to $r \approx 6.8 \mu\text{m}$.

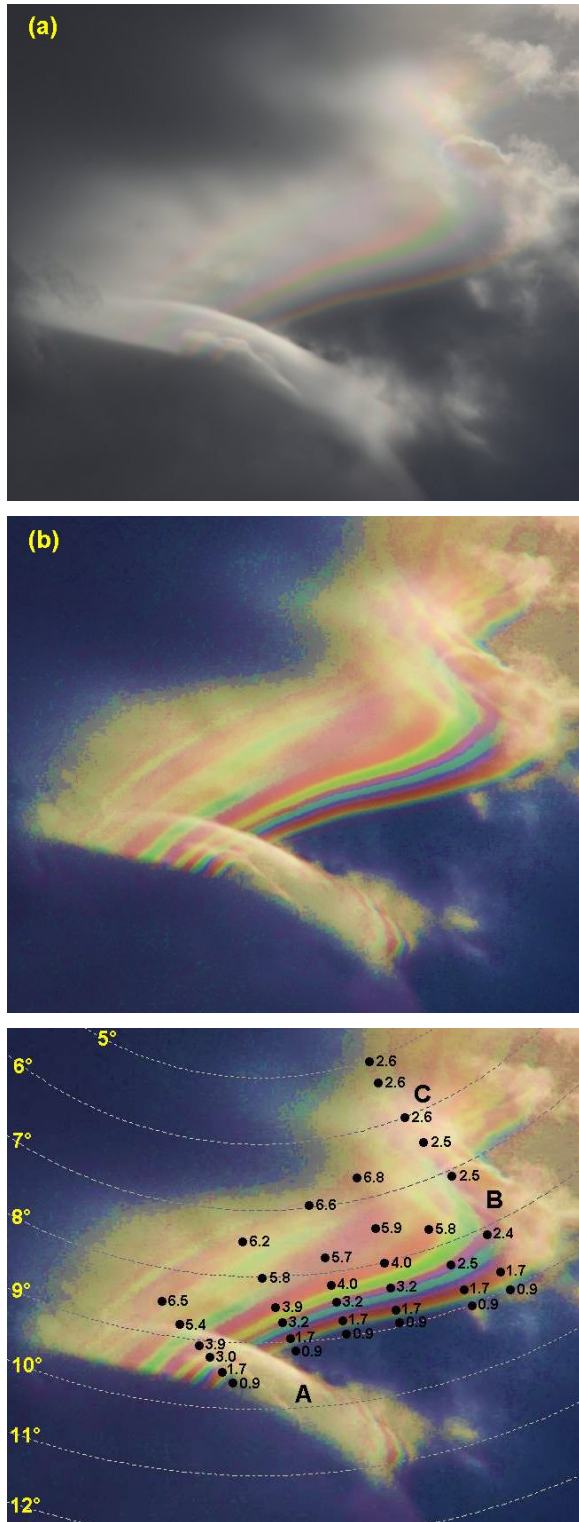


Fig. 6 (a) Unprocessed image recorded at 1303 on 14 November 2021 © Len Hall. (b) As (a) but with color saturation increased by 300% (c) As (b) but showing angular separation θ from the Sun and estimated values of droplet radius r .

Again, most of the colored bands in Fig. 6(c) are aligned with the edges of clouds but there are some interesting exceptions. The upper cloud is screened by two lower cloud streaks: A marks a lower level streak with iridescence at the air entry with the upper cloud iridescent bands seen through it. B marks a second streak that screens the upper cloud more effectively. C marks a reddish band in streak B where the droplets are roughly constant in size with $r \approx 2.6 \mu\text{m}$. The iridescent bands of the upper cloud appear beyond it to the right. The droplet sizes in this streak appear to be due to lifting formation and edge dissipation rather than through-flow. Such anomalies remind us that clouds are 3-dimensional objects and that it is easy to be confused by 2-dimensional images!

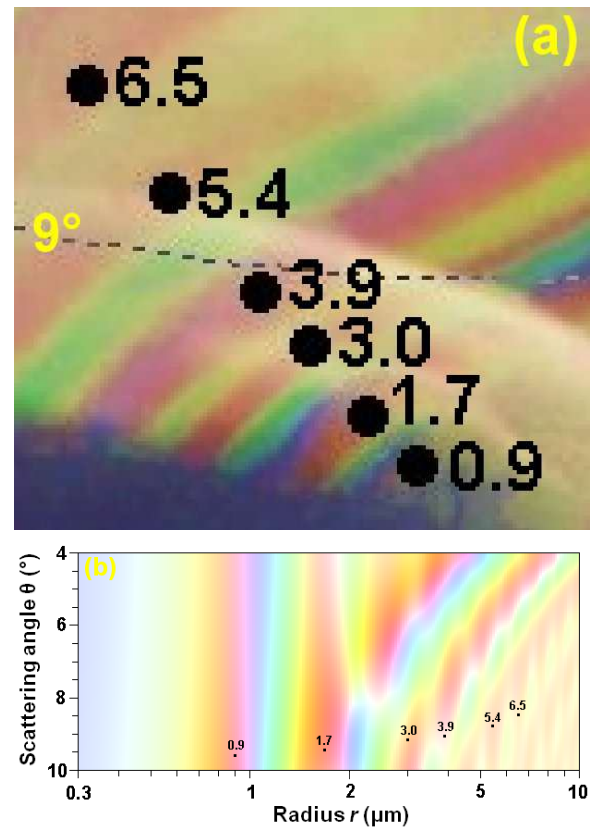


Fig. 7 (a) is an enlarged portion of Fig. 6(c). (b) shows the Mie simulation including the dots from (a).

Examination of Fig. 7(b) shows that the sequence of colors between $r = 0.9 \mu\text{m}$ and $r = 1.7 \mu\text{m}$ is red, violet, blue, cyan, green, yellow and red, which is consistent with Fig. 7(a). Similarly, the sequence of colors between $r = 1.7 \mu\text{m}$ and $r = 3.0 \mu\text{m}$ is red, blue, green, yellow and red in both diagrams. The colors between $r = 3.0 \mu\text{m}$ and $r = 3.9 \mu\text{m}$ are dominated by a distinct yellow band in Fig. 7(a), whereas Fig. 7(b) shows only a hint of yellow. The colors between $r = 3.9 \mu\text{m}$ and $r = 5.4 \mu\text{m}$ are red,

yellow, green, yellow and red in both diagrams. Between $r = 5.4 \mu\text{m}$ and $r = 6.5 \mu\text{m}$, the colors are not easily distinguished in either diagram.

The close agreement between the color sequences in Figs. 7(a) and 7(b) gives us confidence to assert that iridescent bands of colour on clouds are caused by the droplet sizes increasing with distance from the edges of clouds.

In general, our estimates of droplet radius r are subject to two types of error: the angular distance θ from the sun may be slightly incorrect and the extraction of data from Fig. 2(b) is subject to human error. As shown by the near-vertical lines of color in Fig. 2(b), errors in θ have little or no effect on r when $\theta < 10^\circ$. For larger values of θ , it is much more difficult to interpret Fig. 2(b) because bands of color are no longer distinct and they also vary rapidly with r and θ . Consequently, our estimates of the absolute values of r may be in error by up to 10%.

5. CONCLUSIONS

Iridescence in clouds typically appears as colored bands aligned with the edges of clouds or as haphazard patches of color. This paper uses Mie theory simulations to demonstrate that such effects are due to near-forward scattering of sunlight by small spherical water droplets in clouds.

A major problem in investigating iridescence is that most photographers understandably avoid including the Sun in their images of iridescence: this omission means that we rarely know the angular separation θ from the Sun, which obviously hinders scientific analysis of such photographs. This paper describes the use of indirect techniques to determine the position of the Sun even when it does not appear in the photographs.

Detailed analysis of photographs shows that iridescence is typically caused by droplets of radius $0.8 \mu\text{m} < r < 15 \mu\text{m}$ and confirms that the colored bands are due to gradients in droplet size at the edges of clouds.

Disclosures. The authors declare no conflicts of interest.

Funding. No external funding was provided for this project.

Data availability. Data underlying the results presented in this paper are not publicly available at this time but may be obtained from the authors upon reasonable request.

APPENDIX

Assume that the camera produces images which are H pixels wide and V pixels high (e.g. 1920×1080 pixels). The top left pixel is $(0, 0)$, the bottom right pixel is $(H - 1, V - 1)$.

For a lens of focal length F mm (35 mm equivalent), the scale factor $s = H \times F / 36$.

Assume that a known landmark is seen on the image at (x_1, y_1) pixels and that it has an elevation ϕ_1 (measured in degrees above the horizontal) and azimuth λ_1 (measured in degrees east of true north) relative to the camera position.

Our first objective is to determine the elevation ϕ_0 and azimuth λ_0 of the center of the image (x_0, y_0) where $x_0 = (H - 1)/2$ and $y_0 = (V - 1)/2$

$$\text{Let } d_x = x_1 - x_0 \text{ and } d_y = y_1 - y_0. \\ \alpha = \arctan[d_x / d_y]$$

$$\text{If } d_x < 0 \text{ then } \alpha = \alpha + 180^\circ$$

$$\delta = \arctan [(d_x^2 + d_y^2)^{1/2} / s]$$

$$\varepsilon = \arcsin[\sin(\delta) \cos(\alpha)]$$

$$\beta = \arccos[\cos(\delta) / \cos(\varepsilon)]$$

$$\phi_0 = \phi_1 - \varepsilon$$

$$\lambda_0 = \lambda_1 - \beta$$

After determining the elevation ϕ_{Sun} and azimuth λ_{Sun} at the time of each photograph by using <https://gml.noaa.gov/grad/solcalc/azel.html>, the next step is to calculate the Sun's position on the image $(x_{\text{Sun}}, y_{\text{Sun}})$ as measured in pixels using the following equations:

$$\delta_{\text{Sun}} = \arccos[\sin(\phi_0) \sin(\phi_{\text{Sun}}) \\ + \cos(\phi_0) \cos(\phi_{\text{Sun}}) \cos(\lambda_0 - \lambda_{\text{Sun}})]$$

$$d_2 = s \tan(\delta_{\text{Sun}})$$

$$\tau = \arccos[(\sin(\phi_0) - \sin(\phi_{\text{Sun}}) \cos(\delta_{\text{Sun}})) \\ / (\cos(\phi_{\text{Sun}}) \sin(\delta_{\text{Sun}}))]$$

$$x_{\text{Sun}} = x_0 + d_2 \sin(\tau)$$

$$y_{\text{Sun}} = y_0 - d_2 \cos(\tau)$$

REFERENCES

1. L. Cowley, P. Laven and M. Vollmer, "Rings around the sun and moon: coronae and diffraction," *Physics Education*, **40**, 51-59 (2005).
2. P. Laven, "Re-visiting the atmospheric corona," *Appl. Opt.* **54**, B46-B53 (2015).
3. J. Lock and L. Yang, "Mie theory model of the corona," *Appl. Opt.* **30**, 3408-3414 (1991).
4. S. D. Gedzelman and J. A. Lock, "Simulating coronas in color," *Appl. Opt.* **42**, 497-504 (2003).
5. P. Laven, "Simulation of Rainbows, Coronas, and Glories by use of Mie Theory," *Appl. Opt.* **42**, 436-444 (2003).
6. P. Laven, "Simulation of rainbows, coronas and glories using Mie theory and the Debye series," *J. Quant. Spectrosc. Radiat. Transfer* **89**, 257-269 (2004).

7. J. A. Shaw and P. J. Neiman, "Coronas and iridescence in mountain wave clouds," *Appl. Opt.* **42**, 476–485 (2003).
8. P. Laven, "Iridescent clouds and distorted coronas," *Appl. Opt.* **56**, G20 (2017).
9. International Association for the Properties of Water and Steam, "R9-97: Release on the Refractive Index of Ordinary Water Substance as a Function of Wavelength, Temperature and Pressure", <https://iapws.org/documents/release/Rindex>.
10. H. C. van de Hulst, *Light Scattering by Small Particles* (Dover, 1981), reprint of 1957 edition. (Section 13.41).
11. C. D. Whiteman, *Mountain Meteorology: Fundamentals and Applications* (Oxford University, 2000).
12. Z. Cui, A. M. Blyth, K. N. Bower, J. Crosier, and T. Choularton, "Aircraft measurements of wave clouds," *Atmos. Chem. Phys.* **12**, 9881–9892 (2012).
13. W. Mordy, "Computations of the growth by condensation of a population of cloud droplets," *Tellus* **11**, 17–43 (1959).